Effects of topography and Earth's rotation on the oblique interaction of internal solitary-like waves in the Andaman Sea

Shimizu, Kenji

Nakayama, Keisuke

(Citation)
Journal of Geophysical Research: Oceans,122(9):7449-7465

(Issue Date)
2017-09

(Resource Type)
journal article

(Version)
Version of Record

(URL)
https://hdl.handle.net/20.500.14094/90006776

AGU PUBLICATIONS

JGR

Journal of Geophysical Research: Oceans

RESEARCH ARTICLE

10.1002/2017JC012888

Key Points:

- Three-dimensional simulations confirm nonlinear enhancement of ISW amplitude by oblique ISW interaction in realistic oceanic conditions
- Modeled oblique ISW interaction is approximately consistent with extended Miles theory
- Topography and Earth's rotation have small and considerable effects on process of oblique ISW interaction, respectively

Correspondence to:
K. Shimizu,
kenji.shimizu.rc@gmail.com

Citation:
Shimizu, K., and K. Nakayama (2017), Effects of topography and Earth's rotation on the oblique interaction of internal solitary-like waves in the Andaman Sea, *J. Geophys. Res. Oceans*, *122*, 7449–7465, doi:10.1002/2017JC012888.

Received 15 MAR 2017
Accepted 23 AUG 2017
Accepted article online 30 AUG 2017
Published online 15 SEP 2017

Effects of topography and Earth's rotation on the oblique interaction of internal solitary-like waves in the Andaman Sea

Kenji Shimizu[1,2] **and Keisuke Nakayama**[1]

[1]Graduate School of Engineering, Kobe University, Kobe, Japan, [2]Formerly at CSIRO Oceans and Atmosphere, Perth, Western Australia, Australia

Abstract High-resolution three-dimensional MITgcm simulations and an extended Miles theory are used to investigate the oblique interaction of internal solitary-like waves (ISWs) in the Andaman Sea. Oblique solitary-wave interaction is well studied in various fields of physics; however, this process in the ocean has seldom been investigated, despite the observations of its surface signature by remote sensing and potential fourfold increase of ISW amplitude by the development of a (Mach) stem. This study confirms the development of stem-like ISWs under realistic oceanic conditions. The modeled interaction is found to be approximately consistent with the Miles theory extended to unequal incident-wave amplitudes and small-but-finite incident angles. Although topography does not appear to affect the process in the deep part of the Andaman Sea, substantial topographic amplitude variation along the wave trough needs to be adjusted before comparisons with the theory. Earth's rotation has a small effect on ISW propagation due to the low latitude (≈9°N), but it does slow down the growth of stem-like ISWs. Potential observation of the process by the next-generation wide-swath satellite altimeter is discussed.

1. Introduction

Internal solitary-like waves (ISWs) are often observed in marginal seas and on continental shelves [e.g., *Jackson*, 2004, 2007]. They typically have large amplitude, short wavelength, and short period of the order of 10–100 m, 100 m to 10 km, and 10 min to 1 h, respectively [*Osborne and Burch*, 1980; *Holloway et al.*, 1997; *Scotti and Pineda*, 2004; *Klymak et al.*, 2006; *Xie et al.*, 2013]. ISWs are important, for example, as an energy pathway from internal tides to turbulence [e.g., *Lamb*, 2014], as a cause of sediment resuspension [e.g., *Klymak and Moum*, 2003] and acoustic wave refraction [e.g., *Reeder et al.*, 2010], and as a factor affecting offshore structures and operations [*Osborne and Burch*, 1980; *Hyder et al.*, 2005]. In other fields of physics, such as surface water waves and plasma, it is well known that the oblique interaction of two solitary waves could enhance the amplitude by a factor of up to 4; however, this process has seldom been investigated for ISWs in the ocean despite its potential importance. Here we use high-resolution three-dimensional (3-D) MITgcm simulations to investigate oblique ISW interaction under realistic oceanic conditions.

Solitary waves have a strong tendency to preserve their "identity" (e.g., amplitude and shape) through collision, which led *Zabusky and Kruskal* [1965] to coin the term "soliton." There is, however, an exception: their oblique interaction at a small incident angle. *Miles* [1977] developed the original theory for the oblique reflection of a solitary wave on a reflective wall. This process at a small incident angle is analogous to the Mach reflection of shocks in hypersonic flows, and it is equivalent to the oblique interaction of two incident solitary waves with equal amplitude. If the incident angle is smaller than a critical angle, the oblique interaction develops a third solitary wave called a (Mach) stem, which could have an amplitude up to 4 times the incident-wave amplitude (i.e., twice the superposition). For example in Figure 1a, the interaction of two plane incident waves with unequal amplitudes, labeled as [1,3] and [2,4], produces a stem, labeled as [1,4]. The length of a stem increases with time (Figure 1b). If the incident angle is much larger than the critical angle, the incident waves are nearly superposed, except for a small amplitude increase and phase shift near the interaction point (Figure 1d). If the incident angle is larger than but close to the critical angle, the phase shift becomes so large that an approximately plane third wave appears to develop in the interaction region (Figure 1c). Although this apparent third wave resembles a stem, it is not a stem because its length does not increase with time. Note, however, that it is not always possible to distinguish such a wave from a stem in practical applications. In this study, we use the term "stem-like" wave to refer to the third wave developed

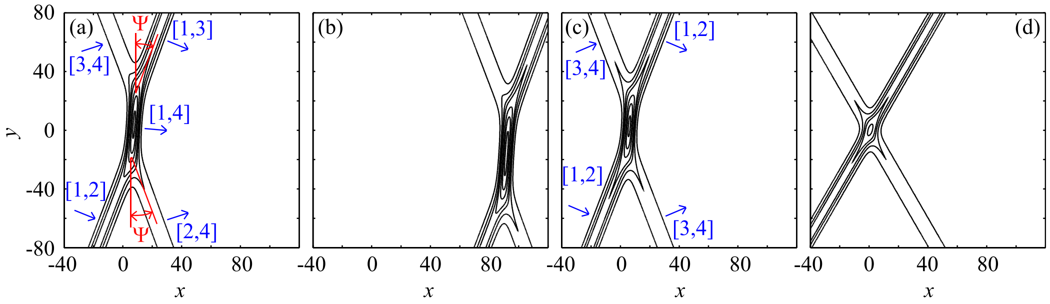

Figure 1. Scaled analytical solutions to KP equation for (3142)-type and O-type interactions, which are simple cases with and without Mach-stem development, respectively. (a) (3142)-type interaction at $\Psi = 20°$ and $t = 0$, (b) that at $\Psi = 20°$ and $t = 600$, (c) O-type interaction at $\Psi = 21°$ and $t = 0$, and (d) that at $\Psi = 30°$ and $t = 0$, where Ψ is the incident angle defined as in Figure 1a, and t is the time. Arrows indicate propagation direction, and $[i, j]$ indices are used to specify solitary waves. Contour lines show amplitude from 0.025 to 0.1 at 0.025 intervals, and then 0.15 to 0.30 at 0.05 intervals. Incident-wave amplitudes are $A_1 = 0.05$ and $A_2 = 0.10$, yielding critical angle of 20.9°. Extended Miles interaction parameter κ is 0.954, 1.01, 1.51 in Figures 1a, 1b; 1c; and 1d, respectively. See Appendix A for scaling of variables and the meaning of $[i, j]$ indices.

by the oblique interaction. Despite the long history of research on oblique solitary-wave interaction, particularly in the field of surface water waves [*Funakoshi*, 1980; *Melville*, 1980; *Miles*, 1980; *Tanaka*, 1993] and plasma [e.g., *Nakamura*, 1982; *Lonngren*, 1983], it is relatively recent that the Miles theory was corrected and then empirically extended to small-but-finite incident angles (see section 2.1 for the details), based on laboratory experiments of surface solitary waves [e.g., *Kodama*, 2010; *Yeh et al.*, 2010; *Li et al.*, 2011].

For internal waves, oblique solitary-wave interaction has received less attention in general and even less in oceanography, although aerial photographs and satellite images show surface signatures characteristic of stem-like ISWs [e.g., *Maxworthy*, 1980; *Helfrich and Melville*, 2006; *New et al.*, 2013]. This is partly because of difficulties in satisfying requirements for both horizontal and temporal coverage and resolution in underwater measurements and 3-D simulations. We are aware of only one experimental study confirming stem-like ISWs [*Maxworthy*, 1980], and one field-based study [*Wang and Pawlowicz*, 2012] and one satellite-based study [*Xue et al.*, 2013] that compared observations with the Miles theory. Unfortunately, the comparisons were not very successful, and one of the reasons is the use of the original Miles theory, which is now known to be problematic for small-but-finite incident angles [*Yeh et al.*, 2010; *Li et al.*, 2011].

Analyzing oblique ISW interaction in the ocean requires understanding beyond the original Miles theory because of the following additional factors: (1) unequal incident-wave amplitudes, (2) transitional response, (3) finite incident angles, (4) strong nonlinearity, (5) topography, and (6) Earth's rotation. The factor (1) has been taken into account in mathematical studies [e.g., *Segur and Finkel*, 1985; *Kodama*, 2010] of the Kadomtsev-Petviashvili (KP) equation [*Kadomtsev and Petviashivili*, 1970]. The results have been adopted in studies of surface water waves [e.g., *Peterson et al.*, 2003], but not in those of ISWs. The factor (2) arises because both the incident-wave amplitudes and incident angle keep changing for diverging or converging incident waves. For example, as the distance from the source r increases, the amplitudes and incident angle for two cylindrical solitary waves decrease as $r^{-2/3}$ [e.g., *Miles*, 1978] and $\arcsin(d/2r)$, respectively (d is the distance between the sources). Such transitional response has been studied in plasma [e.g., *Ze et al.*, 1980; *Tsukabayashi and Nakamura*, 1981; *Kako and Yajima*, 1982], and *Kaup* [1981] estimated the time scale for stem-wave growth for spherical solitary waves. The factor (3) can be partly accounted for by the empirical extension to small-but-finite incident angles by *Yeh et al.* [2010] and *Li et al.* [2011]. More thorough treatment would require the application of the recent theory by *Kodama and Yeh* [2016] to ISWs. The effects of the factor (4) have been studied by *Oikawa and Tsuji* [2006] and *Tsuji and Oikawa* [2007] using the KP equation with strong (cubic) nonlinearity (introduced in section 2.1). The effects of the factors (5) and (6) on oblique ISW interaction do not appear to have been investigated. The presence of topography and Earth's rotation makes it necessary to investigate whether the oblique interaction causes nonlinear enhancement of ISW amplitude in the ocean, and whether the existing theory is sufficient. We use the term solitary-like waves in the presence of Earth's rotation because it destroys an essential property of solitary waves [e.g., *Grimshaw et al.*, 2014].

As a first step to quantitatively investigate oblique ISW interaction in the ocean, we aim to demonstrate that stem-like ISWs do develop under realistic oceanic conditions, and to investigate the effects of topography and Earth's rotation. To do so, we use fully nonlinear and nonhydrostatic 3-D numerical simulations of the generation and subsequent propagation of ISWs, which became feasible relatively recently [*Guo et al.*, 2011; *Zhang et al.*, 2011; *Vlasenko et al.*, 2014]. We take the Andaman Sea as an example because it is one of the well-known regions where large-amplitude ISWs are generated from multiple sites [*Osborne and Burch*, 1980; *Jackson*, 2004; *Hyder et al.*, 2005]. Adapting the results from mathematics and different fields of physics to ISWs, we then compare the modeled interaction with the Miles theory extended to unequal incident-wave amplitudes and small-but-finite incident angles, considering transitional response. We apply only the empirical extension for small-but-finite incident angles by *Yeh et al.* [2010] and *Li et al.* [2011] because the application of the theory by *Kodama and Yeh* [2016] to ISWs in the ocean would require further theoretical studies. Although our investigations into the effects of topography and Earth's rotation are rather preliminary, it makes an essential first step by showing that the detailed process-based studies are worthwhile in the future, and by suggesting research directions.

This paper is organized as follows. Section 2 describes some theoretical background, extension of the Miles theory to unequal incident-wave amplitudes, and setup of the numerical model. The results of numerical simulations and the comparisons with the extended Miles theory are presented in section 3. Implications of the results, including research directions in the future, potential impacts of oblique ISW interaction, and potential observation of the process by the next-generation wide-swath satellite altimeter, are discussed in section 4. Section 5 summarizes the conclusions of this study. Appendices provide a summary of the theory of oblique solitary-wave interaction from mathematical studies, and some details of the processing of model outputs.

2. Methods

2.1. KP Equation With Strongly Nonlinear, Topographic, and Coriolis Effects

Analyzing ISWs under realistic oceanic conditions requires us to consider strong nonlinearity, topography, and Earth's rotation. An ISW equation under these effects may be obtained by adding weak topographic and rotational effects [e.g., *Grimshaw et al.*, 2014] and strong (cubic) nonlinearity [e.g., *Tsuji and Oikawa*, 1993] to the KP equation, yielding

$$\frac{\partial}{\partial x}\left(\frac{\partial \eta}{\partial t}+c\frac{\partial \eta}{\partial x}+\alpha\eta\frac{\partial \eta}{\partial x}+\alpha_1\eta^2\frac{\partial \eta}{\partial x}+\beta\frac{\partial^3 \eta}{\partial x^3}+\frac{c}{2Q}\frac{\partial Q}{\partial x}\eta\right)+\frac{c}{2}\left(\frac{\partial^2 \eta}{\partial y^2}-\frac{f^2}{c^2}\eta\right)=0. \tag{1}$$

Here (x, y) are the horizontal coordinates, t is the time, η corresponds to the vertical displacement of isopycnals, c is the phase speed of nonrotating long linear waves, α and α_1 are, respectively, the quadratic and cubic nonlinear coefficients, β is the linear nonhydrostatic dispersion coefficient, f is the Coriolis parameter, and Q represents topographic effects. For internal waves, η, α, α_1, β, and Q are calculated using a vertical mode of interest (see e.g., *Lamb and Yan* [1996], *Holloway et al.* [1999], and *Grimshaw et al.* [2002] for α, α_1, and β; *Holloway et al.* [1997], *Small* [2001a], and *Grimshaw et al.* [2014] for Q). The above equation apparently lacks a lateral topographic term. For mild bottom slopes, lateral topographic effects could be incorporated through the change of ray-tube width calculated using horizontally varying c [e.g., *Small*, 2001b]. Simplified forms of the above equation will be referred to in various parts of this paper.

2.2. Theory for the Oblique Interaction of Solitary Waves With Unequal Amplitudes

The oblique interaction of solitary waves with unequal amplitudes was first studied by perturbation methods [*Johnson*, 1982; *Soomere*, 2004], but general solutions are now available from mathematical studies of the KP equation (i.e., $\alpha_1=Q=f=0$ in (1)) [e.g., *Kodama*, 2010]. In particular, solutions for two types of the oblique interactions, called (3142)-type and O-type interactions, can be put in a simple form that extends the theory of *Miles* [1977] for equal incident-wave amplitudes to unequal amplitudes. The details of the solutions are given in Appendix A, and a summary is given below.

We consider the oblique interaction of two plane incident solitary waves. Assuming the incident-wave amplitudes of A_1 and A_2 ($|A_2| \geq |A_1|$), we introduce the mean and difference of incident-wave amplitudes, $\bar{A}$ and ΔA, defined as

$$\sqrt{\alpha\bar{A}}=\left(\sqrt{\alpha A_2}+\sqrt{\alpha A_1}\right)/2, \tag{2a}$$

$$\sqrt{\alpha\Delta A}=\sqrt{\alpha A_2}-\sqrt{\alpha A_1}, \tag{2b}$$

respectively. Note that A_1 and A_2 can be negative for ISWs, but α keeps the factors in the square roots positive. Important nondimensional parameters of the problem are

$$\kappa=\frac{\tan\Psi}{\sqrt{2\alpha\bar{A}/c}\cos\Psi}, \tag{3a}$$

$$\sigma=\frac{1}{2}\sqrt{\frac{\Delta A}{\bar{A}}}, \tag{3b}$$

where Ψ is half the angle made by the wavenumber vectors of two incident waves (Figure 1a). We call κ the extended Miles interaction parameter. The original Miles theory [*Miles*, 1977] assumed $\tan\Psi\sim\Psi$ (i.e., Ψ needs to be smaller than that in (3a)); however, later studies [*Kodama*, 2010; *Yeh et al.*, 2010; *Li et al.*, 2011] pointed out that this assumption was unnecessary, and added an empirical $\cos\Psi$ factor in (3a) based on experiments on surface water waves. We refer to these modifications that extend the applicable range of Ψ as the extension to small-but-finite incident angles. In the asymptotic state (i.e., after sufficiently long interaction), the amplification factor a_s is given by

$$a_s\equiv\frac{A_s}{\bar{A}}=\begin{cases}(1+\kappa)^2 & \text{for } \sigma<\kappa\leq 1\\ 4\dfrac{1+\sigma^2\sqrt{\delta}}{1+\sqrt{\delta}} & \text{for } \kappa>1\end{cases}, \tag{4a}$$

$$\delta=\frac{\kappa^2-1}{\kappa^2-\sigma^2}, \tag{4b}$$

where A_s is the extreme amplitude in the interaction region. The case $\kappa<\sigma$ does not appear to be well studied and is not included here. This relationship is shown in Figure 2. For incident waves with an equal amplitude ($\sigma=0$), (3a) and (4) reduce to the $\kappa-a_s$ relationship in the Miles theory extended to small-but-finite incident angles.

This simplified version of the general theory illustrates four important points. First, $a_s>2\left(1+\sigma^2\right)$ indicates nonlinear amplification of solitary-wave amplitude because $a_s\sim 2\left(1+\sigma^2\right)$ for large κ. Second, a_s reaches the peak value of 4 at $\kappa=1$. Third, a_s decreases quickly as κ increases from 1. Fourth, the effect of unequal incident-wave amplitudes is relatively weak (e.g., $A_2/A_1=9$ and 81 for $\sigma=0.5$ and 0.8, respectively).

As mentioned in section 1, the above theory can be applied to ISWs by calculating A_1, A_2, A_s, c, and α using vertical modes. We consider only the first baroclinic mode in this study. Its vertical structure is normalized by its maximum value, so that the modal amplitude corresponds to the extreme isopycnal displacement within the water column. We use the convention that an ISW amplitude is negative for a wave of depression.

2.3. Relevant Time Scales

For diverging or converging solitary waves, the oblique interaction does not reach an asymptotic state because the incident-wave amplitudes and incident angle keep changing. Therefore, it is convenient to compare the time scale for the growth of stem-like ISWs, T_g, with the observed interaction time [*Kaup*, 1981; *Gabl*, 1986]. The time scale T_g can be estimated from the KP equation (i.e., (1) with $\alpha_1=Q=f=0$). We assume $\eta=\eta_1+\eta_2+\eta_3$, where η_1 and η_2 are two plane incident solitary waves that individually satisfy the KP equation. Substituting this η into the KP equation, we get

$$\frac{\partial}{\partial x}\left(\frac{\partial\eta_3}{\partial t}+c\frac{\partial\eta_3}{\partial x}+\alpha\eta_3\frac{\partial\eta_3}{\partial x}+\beta\frac{\partial^3\eta_3}{\partial x^3}\right)+\frac{c}{2}\frac{\partial^2\eta_3}{\partial y^2}=-\frac{\partial}{\partial x}\left(\alpha\frac{\partial}{\partial x}\left(\eta_1\eta_2+(\eta_1+\eta_2)\eta_3\right)\right). \tag{5}$$

To estimate the time scale, we assume $\eta_1\approx\eta_2\approx\bar{A}$, and η_3 grows from 0 to $2\bar{A}$ in the interaction region over the time T_g. Evaluating the right-hand-side at the initial state ($\eta_3\approx 0$ and $\Delta x\approx\sqrt{12\beta/(\alpha\bar{A})}$), we get

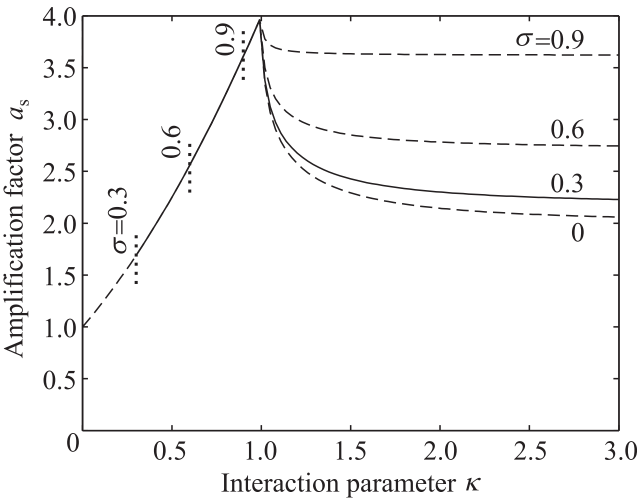

Figure 2. Relationship between extended Miles interaction parameter κ and amplification factor a_s. Solid line shows relationship for $\sigma = 0.3$, and dashed lines for $\sigma = 0.0$, 0.6, and 0.9. Vertical dotted lines indicate lower limit of applicable κ for given σ.

$$T_g \approx 2\sqrt{3}\frac{\beta^{1/2}}{(\alpha\bar{A})^{3/2}}. \tag{6}$$

The important result is the dependence on $\beta^{1/2}(\alpha\bar{A})^{-3/2}$, which agrees with the estimate by *Kaup* [1981] for spherical solitary waves. The coefficient is not very important because actual growth time also depends on the extended Miles parameter κ [*Funakoshi*, 1980; *Li et al.*, 2011].

Another useful time scale is the extinction time T_e, or the time required for ISWs to be extinguished by the Coriolis effect [e.g., *Grimshaw et al.*, 2014]. It is given by

$$T_e \approx \frac{2c}{f^2}\left(\frac{\alpha\bar{A}}{12\beta}\right)^{1/2}. \tag{7}$$

2.4. Numerical Model and Its Configuration

Following previous successful studies [*Vlasenko and Stashchuk*, 2007; *Vlasenko et al.*, 2009, 2014; *Guo et al.*, 2011], we use MITgcm [*Marshall et al.*, 1997] for our ISW modeling. We take into account nonhydrostatic effects, realistic bathymetry represented by the partial cell scheme [*Adcroft et al.*, 1997], and a free surface to allow barotropic tides. We use the Thermodynamic Equation of Seawater-2010 [*McDougall and Baker*, 2011], and sponge zones to dampen outgoing internal waves. To investigate the effects of Earth's rotation, we run "Full Coriolis," "Traditional," and "No Coriolis" cases. The Full Coriolis case includes both vertical and horizontal components of Earth's angular velocity (i.e., including so-called nontraditional effects) [e.g., *Gerkema et al.*, 2008], but the Traditional case includes only the vertical component. The No Coriolis case excludes the Coriolis effect. We expect small effects of Earth's rotation on ISW propagation in the Andaman Sea because the extinction time, $T_e \approx 20$ days (from (7)), is much longer than a typical travel time of ISWs across the deep part of the Andaman Sea, ≈2 days (using $c \approx 2.4$ m s^{-1}, $\alpha \approx -0.012$ s^{-1}, $\beta \approx 4.0 \times 10^5$ m^3 s^{-1}, $\bar{A} \approx 15$ m, and the width of the sea ≈ 200 km at a reference depth of 2300 m). However, the effects of Earth's rotation on oblique ISW interaction need to be investigated separately from those on ISW propagation. We consider nontraditional effects because they are potentially important for flows at low latitudes with significant vertical motion (or nonhydrostaticity), and ISWs in the Andaman Sea satisfy these conditions.

We use two model grids in spherical coordinates covering the whole Andaman Sea. The first grid, with uniform horizontal resolution of 0.005° (≈560 m) except in the sponge zones, is used to locate the occurrence of stem-like ISWs in the whole Andaman Sea. The second grid is used to investigate the most prominent oblique ISW interaction in detail. Its horizontal resolution is 0.0025° (≈280 m) in the region of interest including the generation and interaction sites but becomes gradually coarser near the boundaries. The 0.0025° resolution is typically 1/4 to 1/2 of the minimum horizontal grid resolution required for resolving physical wave dispersion [*Vitousek and Fringer*, 2011]. The vertical grid size is 15 m near the surface and increases with depth in both grids. The total number of grid points, including the sponge zones, is 1320 × 2280 × 45 and 2000 × 1800 × 45 for the coarser and finer resolution grids, respectively.

We use the following input data. Bathymetry is taken from SRTM15_PLUS [*Becker et al.*, 2009]. Horizontally uniform initial stratification is taken from the 2013 version of World Ocean Atlas [*Locarnini et al.*, 2013a, 2013b] (Figures 3a and 3b). The model boundaries are forced by horizontally varying but vertically uniform velocities from the M_2 tide in the TPXO8-atlas [*Egbert and Erofeeva*, 2002]. Although the M_2 tide amplitude is about half of the spring-tide amplitude around the Andaman Sea, we prefer using the M_2 tide to keep sufficient grid resolution in the region of interest (typically 20–30 grid points for the half width of an ISW, or the width where the amplitude is half the maximum, in the finer resolution grid). It

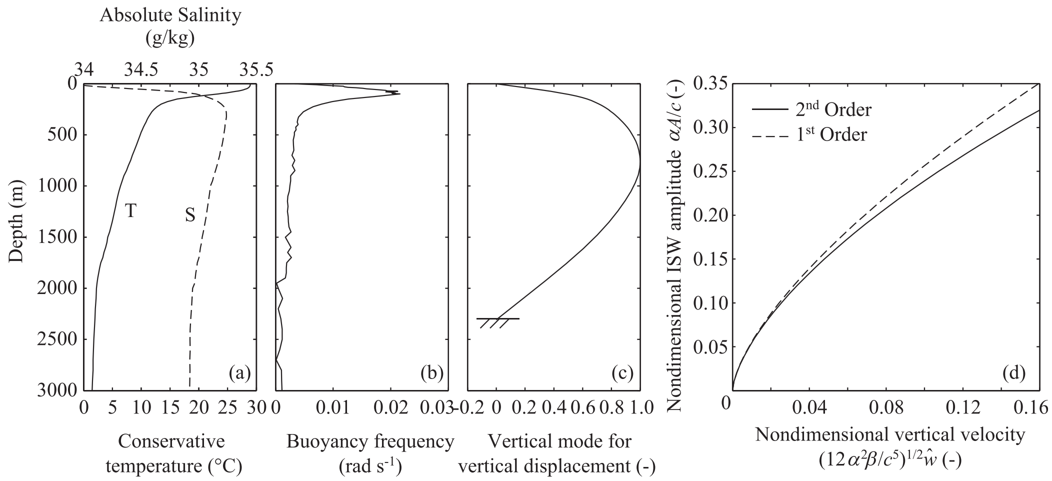

Figure 3. Background state and relationship between vertical velocity and ISW amplitude. (a) Background temperature and salinity used in MITgcm simulations, (b) corresponding buoyancy frequency, (c) corresponding first baroclinic mode at reference water depth, and (d) relationship between nondimensional vertical velocity $\sqrt{12\alpha^2\beta/c^5}\hat{w}$ and nondimensional ISW amplitude $(\alpha A/c)$ at reference water depth of 2300 m, where $c \approx 2.4$ m s^{-1}, $\alpha \approx -0.012$ s^{-1}, $\alpha_1 \approx 4.9 \times 10^{-5}$ m^3 s^{-1}, and $\beta \approx 4.0 \times 10^5$ m^3 s^{-1}. In Figure 3d, curve for "second order" is obtained by including all terms in (B7), and that for "first order" by neglecting last term in (B7).

also keeps the wavelength of the modeled ISWs (typically 8 km) approximately long relative to the water depth ($\approx$2 km).

2.5. Analysis of Model Output

Isopycnal-displacement amplitudes of ISWs are calculated from half hourly model outputs. We prefer calculating an ISW amplitude from vertical velocity because it is easier to identify ISWs, and because vertical velocity at the wave trough across a wave cross section can be used to estimate any local "background" velocity not associated with the ISW. The modal amplitude of vertical velocity $\hat{w}$ is calculated at each horizontal grid point using the first baroclinic mode calculated assuming a locally flat bottom (Figure 3c), following the approach by *Griffiths and Grimshaw* [2007], *Shimizu* [2011], and *Kelly et al*. [2012]. Then, maximum and minimum modal vertical velocities across a wave cross section are related to the ISW amplitude using the analytical soliton solution to the Gardner (or extended Korteweg-de Vries) equation (i.e., $\partial/\partial y = Q = f = 0$ in (1)). We prefer using the undisturbed height of isopycnals as the vertical coordinate in the calculation because it is easier to relate the vertical velocities and isopycnal displacements. Under the initial model stratification and at a typical water depth of 2300 m, the relationship between the ISW amplitude A and $\hat{w}$ shows that neglecting the cubic (strong) nonlinear effects results in overestimation of the largest ISW amplitude in the model by $\approx$10% (Figure 3d). Incident-wave amplitudes A_1 and A_2 are calculated as averages over some segments of the troughs used for quadratic function fitting (see below), and the amplitude of stem-like waves A_s is calculated as the extreme amplitude in the interaction region. The equations used in this calculation are given in Appendix B.

The calculation of incident angle Ψ requires attention because irregularity of ISW shapes under realistic conditions causes relatively large uncertainties. To calculate Ψ, we introduce rotated spherical coordinates (λ, θ) such that approximate origins of the incident waves are located at (0°, -0.8°) and (0°, 0.8°) (Figure 4a). The ISW trough is found as the location where the vertical velocity is equal to the mean of the minimum and maximum vertical velocities across the cross section. Then, quadratic and linear functions are fitted to some segments of the troughs of the two incident waves and the stem-like wave, respectively (green lines in Figure 4b). We calculate the incident angle as the average of the two angles at the intersections (Ψ_1 and Ψ_2 in Figure 4b), and the length of the stem-like ISW as the distance between the intersections. This fitting process is sensitive to the segments of the troughs used. Therefore, we check the sensitivity by randomly choosing lower and upper bounds of the segments within reasonable ranges, chosen based on the shape of the trough lines, amplitude variation along the troughs, and "noise" due to topography (grey bands in Figure 4b). We then use the standard deviation of the incident angle, the length of the stem-like ISW, and the mean incident-wave amplitudes to indicate the uncertainty. Larger ranges are used for the southern

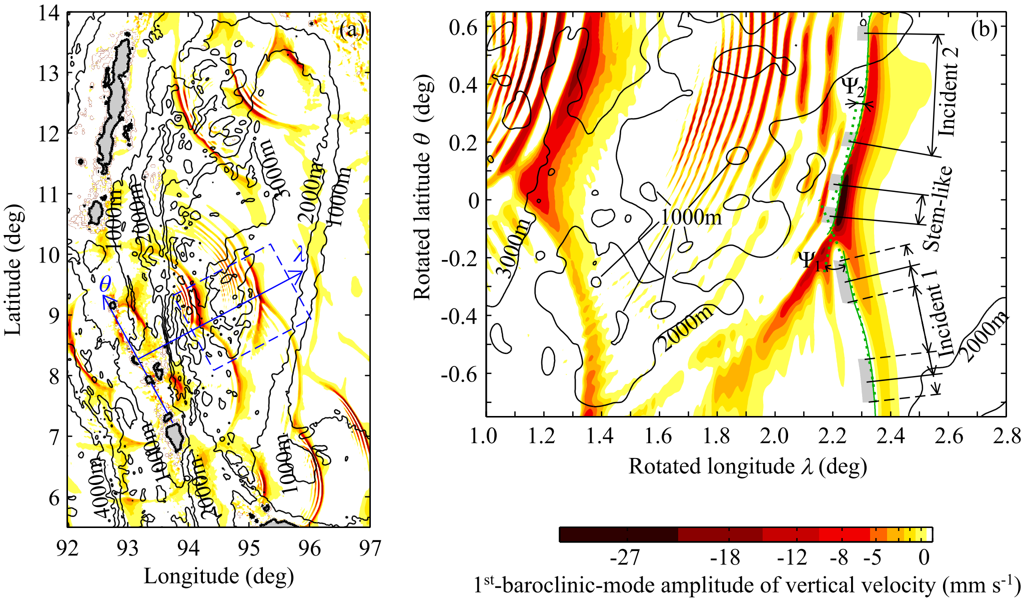

Figure 4. Snapshot of modeled vertical velocity in Andaman Sea (Full Coriolis case). (a) Model output from 0.005° grid and (b) that from 0.0025° grid in region of interest, shown in rotated coordinates (λ, θ) defined in Figure 4a. In Figure 4b, segments labeled "Incident 1," "Incident 2," and "Stem-like" are used for quadratic/linear function fitting, and grey shading indicates ranges for lower and upper boundaries of segments used to estimate uncertainty. Solid and dotted green lines show ISW trough line and examples of fitted quadratic/linear functions, respectively. Incident angle Ψ is calculated as $(\Psi_1+\Psi_2)/2$. Note that only negative velocity is shown and that color scale is nonlinear.

incident wave because few inflection points in the northern part and small curvature in the middle part make the fitting sensitive to the choice of the lower and upper bounds.

3. Results

3.1. Simulation Results

Our simulations produced packets of ISWs of depression, resulting from nonlinear steepening of internal tides generated over the continental slope and the sills between the Andaman and Nicobar Islands. The locations of the generation sites and the shape of the ISW packets (Figure 4a) agree qualitatively with satellite images [*Jackson*, 2004]. *Osborne and Burch* [1980] observed the ISW packets in the southeast part of the Andaman Sea (see 6°N–7°N and east of 95°E in Figure 4a). The observed leading ISW amplitude was $\approx$–60 m during a spring tide at (97.0°E, 6.8°N). The modeled amplitude of the leading ISWs had relatively large gradient along the wave trough, varying between -20 and -40 m within 30 km from the measurement location. Considering that the amplitude of the M_2 tide, used to force the model, is about half of the spring-tide amplitude around the Andaman Sea, and that climatological stratification is used in the model, the modeled ISW amplitude is roughly consistent with observation.

The oblique interaction of the simulated ISWs produced stem-like ISWs, both with and without the Coriolis effect. This suggests robustness of stem-like ISW development under the effects of topography and Earth's rotation. In the following, we use the Full Coriolis case as our base case. We focus on the most prominent stem-like ISW around (95°E, 9°N) (Figure 4b). It was produced by the leading ISWs of two (approximately) cylindrically diverging ISW packets, originating from sills of 160–250 m depth around the Nicobar Islands. Within $\approx$6 h, the peak magnitude of the stem-like ISW amplitude increased from less than 20 m to more than 60 m, and the length increased to $\approx$25 km (Figures 5a and 5b). After reaching the peak, the magnitude decreased due to divergence of the wave trough and damping. Note that one of the causes of the damping is the shedding of dispersive internal waves, which can be seen around $(\lambda, \theta) =$ (1.9°, 0.4°) in Figure 4b.

3.2. Effects of Topography

Although stem-like ISW development was robust under topographic effects, the modeled ISW amplitudes (Figure 5b) showed substantial variation (up to a factor of 2), well correlated with water depth at least in the

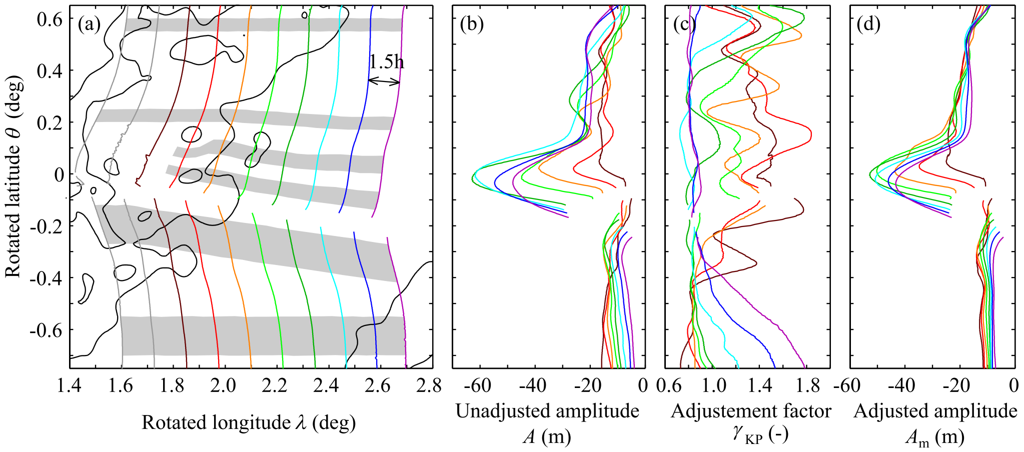

Figure 5. Troughs and amplitudes of modeled ISWs at 1.5 h intervals (Full Coriolis case). (a) Location of ISW troughs, (b) "raw" amplitudes unadjusted for topographic variation A, (c) topographic adjustment factor γ_{KP}, and (d) adjusted amplitudes $A_m = \gamma_{KP} A$. Color indicates correspondence in different panels. In Figure 5a, grey shading indicates ranges for lower and upper bounds of ISW segments used for quadratic/linear function fitting. Isobaths are shown at 1000 m intervals.

lateral (along-trough) direction. This topographic amplitude variation needed to be adjusted before comparing the modeled oblique ISW interaction with the extended Miles theory in section 2.2. We first tried the standard amplitude correction based on the conservation of energy [*Zhou and Grimshaw*, 1989; *Small*, 2001a; *Grimshaw et al.*, 2014], but it was unsuccessful, most likely because it is intended for longitudinal topographic effects. Lateral amplitude variation could be calculated by convergence of ISW ray paths, but ray tracing was not straightforward because more than 20% water-depth change over one ISW in the region of interest (Figure 4b) caused crossing of adjacent rays (i.e., caustics).

Since we were unable to find a suitable theory or method, we decided to adjust the lateral amplitude variation empirically, and looked for a parameter that has a simple and good correlation with the ISW amplitude normalized by its along-trough mean. After some trial and error, we decided to use topographic adjustment based on scaling used to nondimensionalize the KP equation (i.e., $\alpha_1 = Q = f = 0$ in (1)) into a standard form (see (A1) and (A2) in Appendix A):

$$A_m = \gamma_{KP} A, \tag{8a}$$

$$\gamma_{KP} = \left(\frac{\alpha}{c} \frac{c_{ref}}{\alpha_{ref}} \right), \tag{8b}$$

where A is the "raw" ISW calculated as explained in section 2.5, A_m is the amplitude adjusted to a reference depth of 2300 m, and the subscript ref is used to indicate reference values. The factor γ_{KP} correlated well with the "raw" amplitudes (Figures 5b and 5c) and the adjustment removed lateral topographic amplitude variation well (Figure 5d). Conveniently, this result means that the known solutions to the KP equation, which assumes a flat bottom, can be applied in the presence of lateral topographic effects after the above amplitude adjustment.

Since (8) is empirical, we assessed the error by correlating A/A_m against ${\gamma_{KP}}^{-1}$ along the troughs of the incident ISWs, using the along-trough mean of $\gamma_{KP} A$ as an estimate of A_m. The standard error from (8) was $\pm 1.5\%$ (Figure 6a) assuming one degree of freedom for every 0.1°, a typical length scale of topographic features in the SRTM15_PLUS bathymetry for the region (Figure 4b). The correlation between ${\gamma_{KP}}^{-1}$ and A_m^{-1} showed negative and unclear trends for the southern and northern incident ISWs, respectively (Figure 6b). Therefore, the positive trend in Figure 6a was primarily caused by along-trough amplitude variation.

3.3. Comparison With Extended Miles Theory

For comparison with the extended Miles theory in section 2.2, we calculated the extended Miles interaction parameter κ and the amplification factor a_s using the ISW amplitudes adjusted for lateral topographic variation (Figures 5d and 7a). Initially, the oblique interaction of the two incident ISWs did not develop a stem-like ISW because the incident angle was large and κ was clearly larger than 1 (Figures 7b and 7c). However,

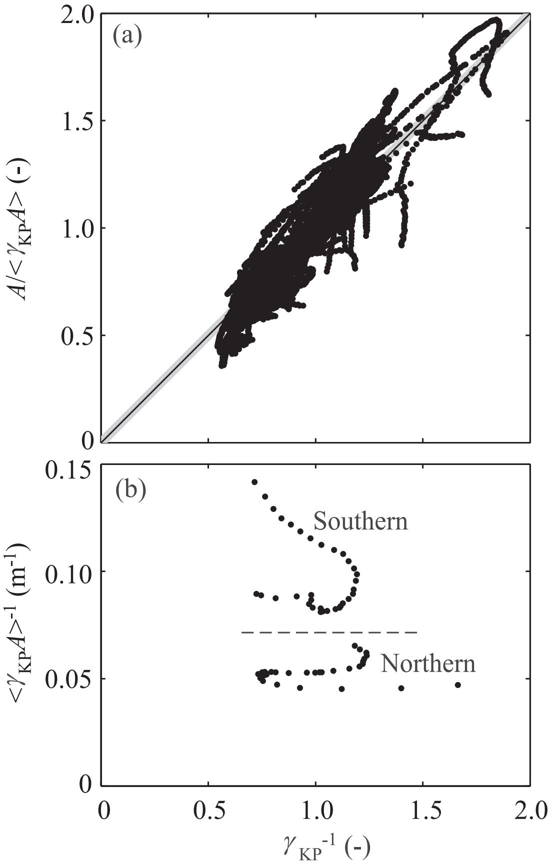

Figure 6. Uncertainty in topographic adjustment of ISW amplitudes (8). (a) Correlation between γ_{KP}^{-1} and $A/\langle\gamma_{KP}A\rangle$, and (b) correlation between γ_{KP}^{-1} and $\langle\gamma_{KP}A\rangle^{-1}$, where angular brackets indicate along-trough average. Data points are taken from every grid point along northern and southern incident ISWs in Full Coriolis case at half-hour intervals over period shown in Figure 5a. In Figure 6a, shading indicates twice the standard error. The slope and intercept are 1.1 ± 0.1 and -0.09 ± 0.3 with the uncertainty calculated as twice the standard error.

divergence of the incident waves gradually reduced the incident angle and κ with time. Once κ reached 0.9–1.3, a stem-like ISW started to grow, and within $\approx$6 h, the length of the stem-like ISW L_s and a_s reached apparent asymptotic values of 20–30 km and 3.6–4.0, respectively (Figures 7c–7e). The growth time agrees well with the estimate from (6), which is 8 h using $\bar{A}_m \approx -15$ m, $\alpha \approx -0.012$ s^{-1}, and $\beta \approx 4.0 \times 10^5$ m^3 s^{-1} at a reference depth of 2300 m. The development phase of the stem-like ISW was approximately consistent with the extended Miles theory considering transitional response and uncertainty in estimating relevant parameters in realistic oceanic conditions (red to green shading in Figure 8).

The amplification factor a_s kept the apparent asymptotic value of 3.6–4.0 even after κ increased to 1.1–1.4 (dark blue and purple shading in Figure 8). During this period, a_s was larger than the value predicted by (4). There are two possibilities for this. One possibility is that once the amplitude of the stem-like ISW became larger than that predicted by (4), the stem-like ISW was released from apparent "forcing" by the incident waves and propagated freely. Such a process was suggested by the free decay of cylindrically diverging stem-like waves in plasma [e.g., *Ze et al.*, 1980; *Tsukabayashi and Nakamura*, 1981]. Another possibility is that the incident and stem-like ISWs kept interacting because strong nonlinearity, which is excluded in the extended Miles theory, increased the κ value corresponding to the maximum a_s (see section 4 for the details).

3.4. Effects of Earth's Rotation

Comparison of the amplitudes in the No Coriolis and Full Coriolis cases showed that the Coriolis effect slowed down the growth of the stem-like ISW (Figures 7a, 7d, and 7e), although the incident-wave amplitudes and incident angle were similar (Figures 7a–7c). This is an interesting result considering the low latitude of the Andaman Sea (the interaction occurring at 9°N) and a consequent small effect of Earth's rotation on ISW propagation. The peak magnitude of the stem-like ISW amplitude also differed by more than 10% (Figure 7a); however, we were unable to determine whether this was caused by insufficient interaction time or reduced maximum a_s. The results of the Traditional case were nearly identical to the Full Coriolis case, showing that the nontraditional effects were unimportant.

4. Discussion

This study investigated oblique ISW interaction under realistic conditions in the Andaman Sea using high-resolution 3-D MITgcm simulations and an extended Miles theory. To our knowledge, this is the first study that has demonstrated approximate consistency between stem-like ISW development under realistic oceanic conditions, and the Miles theory extended to unequal incident-wave amplitudes and small-but-finite incident angles. Looking at the details, however, the stem-like ISW developed when κ tended to be larger than 1 (Figure 8), and peak a_s tended to be slightly larger than 4 in the No Coriolis case (Figures 7c and 7e). Although these deviations from the theory are within the range of uncertainty, there are potential physical

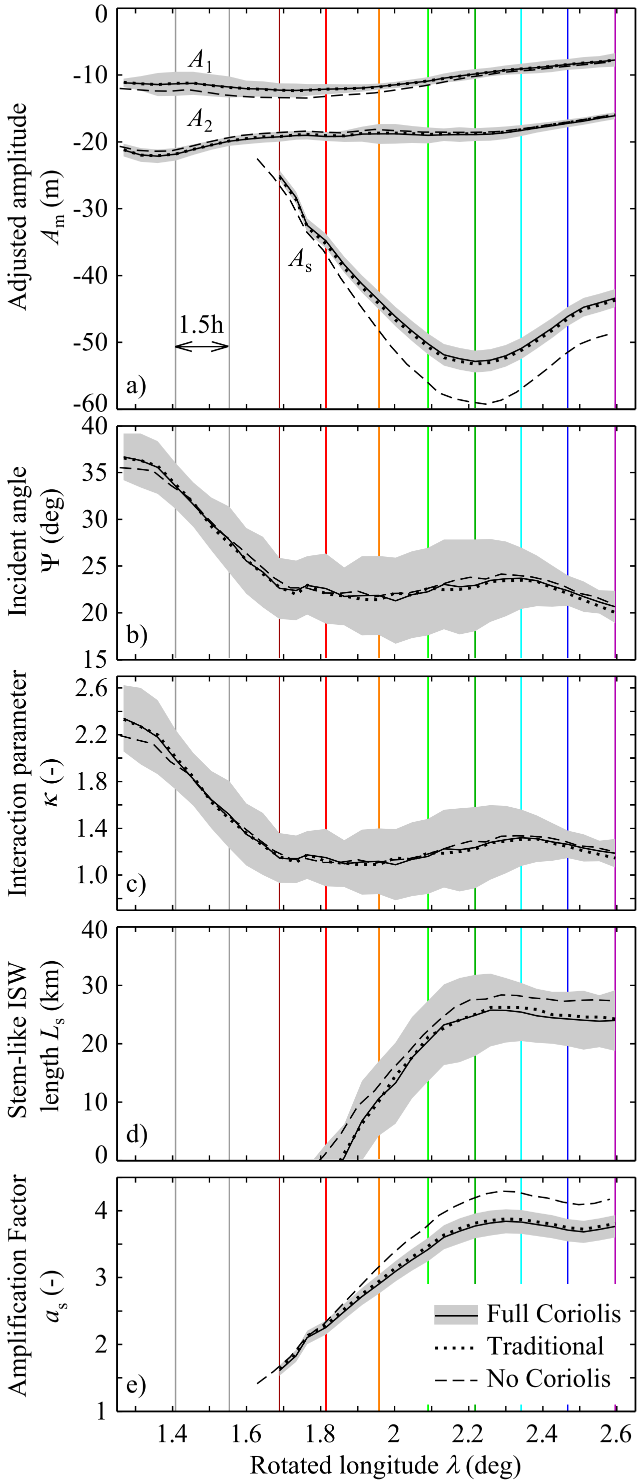

Figure 7. Parameters relevant to oblique ISW interaction. (a) Amplitudes of southern incident ISW A_1, northern incident ISW A_2, and stem-like ISW A_s, (b) incident angle Ψ, (c) extended Miles interaction parameter κ, (d) length of stem-like ISW L_s, and (e) amplification factor a_s. Colored vertical lines correspond to 1.5 h intervals in Figure 5. Shading indicates uncertainty estimated based on twice the standard deviation due to quadratic/linear function fitting and twice the standard error due to topographic amplitude adjustment in Full Coriolis case. Uncertainties in Traditional and No Coriolis cases are similar to Full Coriolis case.

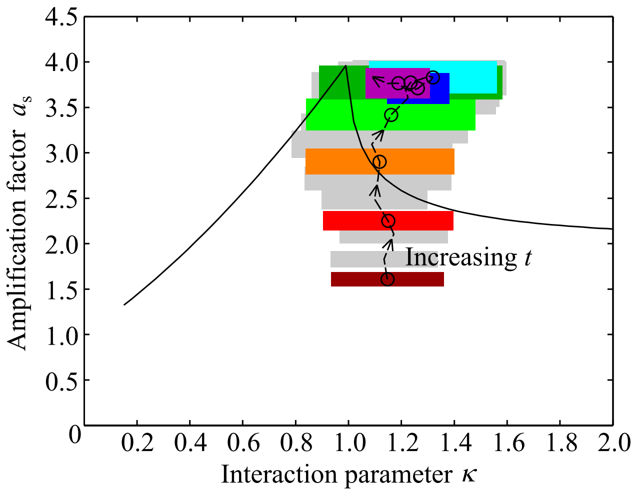

Figure 8. Comparison of relationship between extended Miles interaction parameter κ and amplification factor a_s. Solid line shows extended Miles theory for analyzed interaction using mean σ (=0.15). Dashed line and shading correspond to solid line and shading in Figures 7c and 7e (Full Coriolis case). Direction of increasing time t is indicated by arrows. Colored shading with a circle in middle indicates 1.5 h time intervals, corresponding to colored lines in Figure 5 and colored vertical lines in Figure 7.

reasons for them. *Tsuji and Oikawa* [2007] introduced a nondimensional parameter representing the relative magnitude of the cubic to quadratic nonlinear term in (1), $Q^*=-6\alpha_1 A/\alpha$, and showed that when Q^* increased from 0 to 1, the κ value for the maximum amplification and the maximum a_s decreased by $\approx$20% and $\approx$10%, respectively. A typical value of Q^* was -0.5 in our simulations. Although we are unaware of studies of negative Q^*, strong nonlinearity might be a reason for $\kappa > 1$ during the stem-like ISW development and $a_s > 1$ in No Coriolis case.

One of the important roles of realistic numerical simulations, such as those conducted in this study, is to point out physical factors that are worth further investigation in process-based studies. Although the development of stem-like ISWs was robust under the effects of topography and Earth's rotation at least in the deep part of the Andaman Sea, the influence of Earth's rotation on oblique ISW interaction was considerable. Since the nontraditional effects are unimportant, the effects of Earth's rotation could be studied further by idealized numerical simulations based on the rotation-modified KP equation (i.e., $\alpha_1=Q=0$ in (1)). Furthermore, both realistic and idealized simulations would be needed to investigate quantitatively the effects of Earth's rotation at midlatitudes, where some surface signatures of oblique ISW interaction have been observed by satellites [*Helfrich and Melville*, 2006; *Xue et al.*, 2013]. Topography does not appear to affect the process of oblique ISW interaction, but it induced substantial along-trough amplitude variation. We used an empirical amplitude adjustment in this study, and theoretical studies would be required to understand the lateral topographic effects. Our simulations also suggest the need of including lateral topographic effects in (1), and the potential importance of strong nonlinearity. Further investigation into the effects of strong nonlinearity, topography, and Earth's rotation would be essential to better understand oblique ISW interaction, not only in relatively deep seas at low latitudes, such as the Andaman Sea, but also on shallow continental shelves at midlatitudes.

The result that the nonlinear enhancement of ISW amplitudes can occur in realistic oceanic conditions leads to a number of interesting questions. One of them is the consequences, for example, to mixing, sediment transport, and offshore structures and operations. If we write the amplitude of horizontal velocity induced by ISWs as U, the gradient Richardson number (its value below a critical value indicates linear instability) is roughly proportional to U^{-2}, whereas bottom shear stress and drag force per unit area of underwater structure are roughly proportional to U^2. So fourfold enhancement of horizontal velocity by stem-like ISW development would reduce the gradient Richardson number, and increase bottom shear stress and drag force on offshore structure, by an order of magnitude. In deep water, stem-like ISWs are more likely to remain stable to instability, as in our Andaman Sea simulations. However, they could exert extreme forcing on offshore structures and cause difficulties in offshore drilling operations, which are relevant, for example, to the oil and gas industry in the Andaman Sea. As stem-like ISWs approach shallower water, they are more likely to become unstable and break. The development of stem-like ISWs does not change the total amount of energy available to mixing, but the enhanced amplitudes and relatively short trough lengths could lead to localized, more severe mixing and breaking events. Such events could create submesoscale patches of high primary productivity by bringing nutrients from deeper water, similar to the processes after the interaction of ISWs with submesoscale topographic features [e.g., *Wang et al.*, 2007; *New et al.*, 2013]. Extreme bottom shear stress due to stem-like ISWs would also be important for sediment transport, and the impact could appear as large bed forms [*Reeder et al.*, 2011].

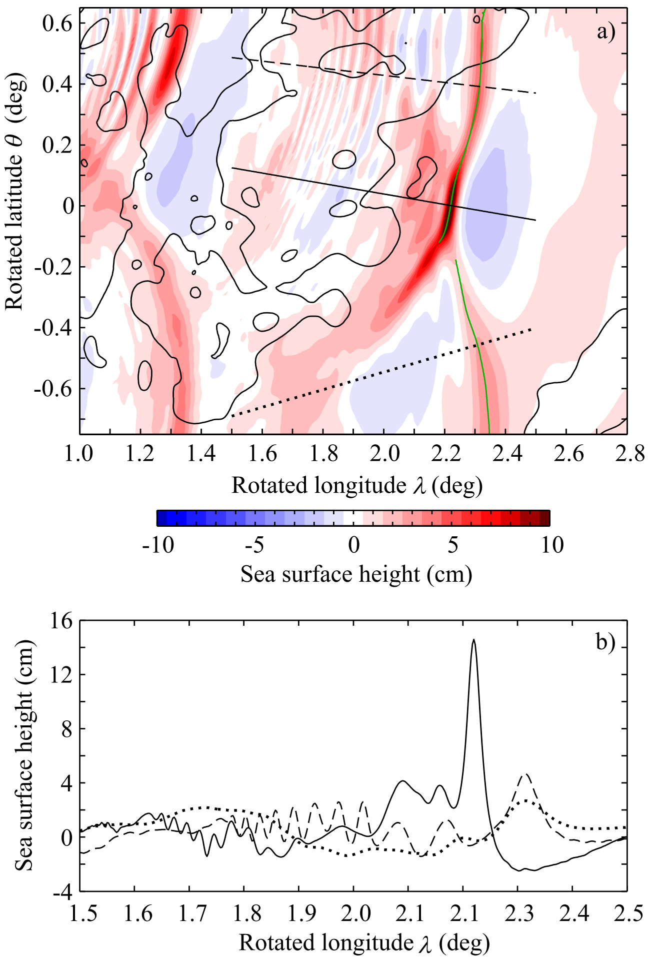

Figure 9. Sea surface height (SSH) expression of modeled oblique ISW interaction under M_2 tidal forcing (Full Coriolis case, amplitude unadjusted for topographic variation). (a) SSH in the region shown in Figure 4b, and (b) profiles of SSH along solid, dashed, and dotted lines shown in Figure 9a. Green line in Figure 9a shows ISW trough line calculated from vertical velocity (same as green line in Figure 4b). Mean sea level and M_2 tide are removed by subtracting mean of modeled SSH time series at each grid point, and then by least-square fitting of sinusoidal function with M_2 tidal frequency to SSH time series.

Another interesting question is the spatial and temporal distributions of oblique ISW interaction, in particular those of nonlinear enhancement of ISW amplitudes. Although it appears difficult to answer this question with the current observational and modeling capabilities, the wide-swath satellite altimeter by the Surface Water and Ocean Topography (SWOT) mission (https://swot.jpl.nasa.gov) might begin to provide part of the answer in the near future. The altimeter is going to provide sea surface height over 120 km swath with planned resolution and accuracy of 1 km and 1 cm, respectively. In comparison, the ISWs analyzed in this study have ~8 km wavelengths and 10–60 m isopycnal-displacement amplitudes, which translate to 3–18 cm surface-displacement amplitudes (Figure 9). Note that the simulations were run only with M_2 tidal forcing, and the forcing during spring tides is about twice as strong around the Andaman Sea. More generally, ISWs in the ocean have wavelengths and surface-displacement amplitudes of the order of 100 m to 10 km and 1–10 cm. Despite the apparent limitation to ISWs with relatively large amplitudes and long wavelengths, the next-generation altimeter might begin to resolve the amplitudes and horizontal shapes of interacting ISWs in large part of the World Ocean. An example from realistic 3-D simulations analyzed in this study, as well as the summary of the theory, would help interpreting the results of satellite observation in the future.

5. Conclusions

This study used 3-D MITgcm simulations and the Miles theory extended to unequal incident-wave amplitudes and small-but-finite incident angles to investigate oblique ISW interaction under realistic conditions in the Andaman Sea. The modeled oblique interaction was found to be approximately consistent with the extended Miles theory. Although the development of stem-like ISW was robust under the effects of topography and Earth's rotation in the deep sea at low latitude (interaction at ≈9°N), topography was found to induce substantial along-trough amplitude variation, and Earth's rotation to slow down the growth of stem-like ISWs.

Appendix A: The Miles Theory for Incident Waves With Unequal Amplitudes

This appendix describes two solutions for the oblique interaction of two solitons with unequal amplitudes. Although the theory is mostly taken from a mathematical study by *Kodama* [2010], we believe it useful to summarize the recent theory from mathematical studies for its application to internal waves.

We consider solutions to the Kadomtsev-Petviashvili (KP) equation (i.e., $\alpha_1 = Q = f = 0$ in (1)) in a standard nondimensional form:

$$\frac{\partial}{\partial x}\left(4\frac{\partial \eta}{\partial t}+6\eta\frac{\partial \eta}{\partial x}+\frac{\partial^3 \eta}{\partial x^3}\right)+3\frac{\partial^2 \eta}{\partial y^2}=0. \tag{A1}$$

Using the superscript * to denote a dimensional variable, the above nondimensional form is derived based on the following scaling in a frame of reference moving with long linear wave speed c^*:

$$x=\sqrt{\frac{c^*}{6\beta^*}}\left(x^*-c^*t^*\right),\ y=\sqrt{\frac{c^*}{6\beta^*}}y^*,\ t=\frac{2c^*}{3}\sqrt{\frac{c^*}{6\beta^*}}t^*,\ \eta=\frac{\alpha^*}{c^*}\eta^*. \tag{A2}$$

Note that the amplitude scale in the last relationship is used for the lateral topographic amplitude adjustment (5). The single soliton solution to (A1) can be written as [*Kodama*, 2010]

$$\eta=\frac{1}{2}\left(k_j-k_i\right)^2\operatorname{sech}^2\left(\frac{1}{2}\left(\theta_j-\theta_i\right)-\theta_0\right), \tag{A3a}$$

$$\theta_i=k_i x+k_i^2 y-k_i^3 t, \tag{A3b}$$

where θ_0 is the phase shift, and $k_j > k_i$ is assumed. Hereafter, the subscript [*i,j*] indicates a variable associated with a soliton solution formed with parameters $\left(k_i, k_j\right)$, called an [*i,j*]-soliton [*Kodama*, 2010]. The amplitude and angle of an [*i, j*]-soliton are respectively given by

$$A_{[i,j]}=\frac{1}{2}\left(k_j-k_i\right)^2, \tag{A4a}$$

$$\tan\Psi_{[i,j]}=\left(k_j^2-k_i^2\right)/\left(k_j-k_i\right)=k_j+k_i. \tag{A4b}$$

The KP equation supports many solutions for oblique soliton interaction, but here we consider solutions for two relatively simple interactions, called (3142)-type and O-type interaction.

A1. (3142)-Type Interaction

If the incident angle is relatively small but not too small, the oblique interaction of two solitons produces a Mach stem. The (3142)-type interaction is a simple case that produces a Mach stem. There are five solitons in this solution (Figure 1a), and the four k_i parameters are determined by the amplitudes and angles of the incident solitons. Putting the k_i parameters in increasing order, the incident (or colliding) solitons are [1,3]-soliton and [2,4]-soliton, and their interaction produces a Mach stem, [1,4]-soliton, and so-called reflected (or collided) soliton, [1,2]-soliton and [3,4]-soliton. Note that this solution is unsteady even when seen from an appropriate moving frame of reference, but the solution reaches an asymptotic state, in which the amplitudes reach constant values and the stem length increases linearly with time (compare Figures 1a and 1b).

Without loss of generality, we assume the amplitudes and angles of the incident waves to be $A_{[1,3]}=A_2$, $A_{[2,4]}=A_1(\leq A_2)$, and $-\Psi_{[1,3]}=\Psi_{[2,4]}=\Psi$. This determines the four k_i parameters from (A4). For later convenience, we introduce the mean amplitude $\bar{A}$ and amplitude difference ΔA, defined as

$$\sqrt{\bar{A}}=\left(\sqrt{A_2}+\sqrt{A_1}\right)/2, \tag{A5a}$$

$$\sqrt{\Delta A}=\sqrt{A_2}-\sqrt{A_1}, \tag{A5b}$$

as well as the parameters

$$\kappa=\frac{\tan\Psi}{\sqrt{2\bar{A}}}, \tag{A6a}$$

$$\sigma=\frac{1}{2}\sqrt{\frac{\Delta A}{\bar{A}}}. \tag{A6b}$$

The parameter κ extends the definition of the interaction parameter by *Miles* [1977], later corrected by e.g., *Kodama* [2010] and *Yeh et al.* [2010], to incident waves with unequal amplitudes. The solutions for the stem and reflected waves are calculated from the k_i parameters of the interacting solitons, (A3), and (A4). The amplitude and angle of the stem is

$$A_{[1,4]}=\frac{1}{2}\left(k_4-k_1\right)^2=\bar{A}(1+\kappa)^2, \tag{A7a}$$

$$\tan\Psi_{[1,4]}=k_4+k_1=-\sqrt{2\bar{A}}\sigma, \tag{A7b}$$

and those for the reflected solitons are

$$A_{[1,2]}=\frac{1}{2}\left(k_2-k_1\right)^2=\bar{A}(\kappa+\sigma)^2, \tag{A8a}$$

$$A_{[3,4]}=\frac{1}{2}\left(k_4-k_3\right)^2=\bar{A}(\kappa-\sigma)^2, \tag{A8b}$$

$$\tan\Psi_{[3,4]}=-\tan\Psi_{[1,2]}=\sqrt{2\bar{A}}. \tag{A8c}$$

Note that the (3142)-type interaction is possible when $\sigma<\kappa<1$. This quantifies the "relatively small but not too small" incident angle assumed at the beginning.

A2. O-Type or (2143)-Type Interaction

When the incident angle is relatively large (i.e., $\kappa>1$), two solitons interact without producing a Mach stem. The O-type interaction is a simple case of such an interaction. Again putting the k_i parameters in increasing order, there are [1,2]-soliton and [3,4]-soliton in the solution (Figure 1c). The solitons, however, have phase shifts due to the interaction, and the solution around the interaction point deviates from the soliton solution (A3). This solution is steady when seen from an appropriate moving frame of reference.

Without loss of generality, we assume $A_{[1,2]}=A_2$, $A_{[3,4]}=A_1(\leq A_2)$, and $-\Psi_{[1,2]}=\Psi_{[3,4]}=\Psi$. The solution around the interaction point cannot be obtained using the simplified approach based on the single soliton solution (A3) and k_i parameters. The full solution shows that the maximum amplitude near the interaction point is

$$A_{\max}=A_1+A_2+2\frac{1-\sqrt{\delta}}{1+\sqrt{\delta}}\sqrt{A_1A_2}=4\bar{A}\left(\frac{1+\sigma^2\sqrt{\delta}}{1+\sqrt{\delta}}\right). \tag{A9}$$

Note that the O-type interaction is possible when $\kappa>1$.

A3. Miles Theory Extended to Unequal Incident-Wave Amplitudes and Small-But-Finite Incident Angle

Defining the amplification factor a_s as the maximum amplitude in the interaction region relative to $\bar{A}$, (A7) and (A9) yield the Miles theory extended to unequal incident-wave amplitudes. It can be further extended to small-but-finite incident angle by applying the empirical $\cos\Psi$ factor to (A6a) [*Kodama*, 2010; *Yeh et al.*, 2010; *Li et al.*, 2011], yielding (3a).

Appendix B: Calculating ISW Amplitude From Vertical Velocity

This appendix describes the method used to calculate internal solitary-like wave (ISW) amplitude from modeled vertical velocity using the analytical soliton solution to the Gardner equation (i.e., $\partial/\partial y=Q=f=0$ in (1)). The calculation is done in the following three steps.

First, we introduce the standard vertical mode decomposition (or the generalized Fourier decomposition) of isopycnal-displacement field η and vertical velocity field w at horizontal location $\vec{x}$ [e.g., *Benney*, 1966; *Gill*, 1982]:

$$\eta(\vec{x},Z,t)=\sum_n\phi_n(\vec{x},Z)\hat{\eta}_n(\vec{x},t), \tag{B1a}$$

$$w(\vec{x},Z,t)=\sum_n\phi_n(\vec{x},Z)\hat{w}_n(\vec{x},t), \tag{B1b}$$

where Z is the undisturbed height of isopycnals, ϕ_n is the vertical mode calculated using the local water depth $H(\vec{x})$ (e.g., Figure 3c), and the subscript n is the modal index. Assuming the Boussinesq approximation, the vertical modes satisfy the orthogonality relationship [e.g., *Gill*, 1982]:

$$\phi_m^s g \phi_n^s + \int_{-H}^{0} \phi_m N^2 \phi_n dZ = \frac{c_n^2}{h_n}\delta_{mn}, \tag{B2}$$

where c_n is the phase speed of nth mode, $N(Z)$ is the background buoyancy frequency (e.g., Figure 3b), δ_{mn} is the Kronecker delta, and the superscript s denotes the value at the surface. The variable h_n is the normalization factor of nth mode, calculated by setting $m=n$ in the above equation. From a known vertical velocity field $w(\vec{x}, Z, t)$, we calculate $\hat{w}_n$ as

$$\hat{w}_n = \frac{h_n}{c_n^2}\left(\phi_n^s g w^s + \int_{-H}^{0} \phi_n N^2 w dZ\right). \tag{B3}$$

Note that this is a general relationship from the generalized Fourier theory and is applicable irrespective of the strength of nonlinearity and nonhydrostaticity, as seen in the spectral approach by *Benney* [1966]. Hereafter, we consider only a particular mode of interest, and omit the subscript.

Second, we calculate isopycnal-displacement amplitude $\hat{\eta}$ from the amplitude of vertical velocity $\hat{w}$. In the horizontal coordinate moving with the ISW speed $\xi = x - c_{sw}t$, vertical velocity and isopycnal displacement are related as $w = -c_{sw}(1+\partial\eta/\partial Z)^{-1}(\partial\eta/\partial\xi)$ [*Benjamin*, 1966]. Assuming that only the mode of interest has nonzero amplitude at 0th (linear) order, projection of the above relationship onto the mode of interest using (B1) and (B2) yields, to first order in nonlinear effects:

$$\hat{w} \sim -c_{sw}\left(1 - \frac{N_B}{h}\hat{\eta}\right)\frac{\partial\hat{\eta}}{\partial\xi}, \tag{B4a}$$

$$N_B = \frac{h^2}{c^2}\left(\phi^s g\left(\frac{\partial\phi}{\partial Z}\right)_{Z=0}\phi^s + \int_{-H}^{0} \phi N^2 \frac{\partial\phi}{\partial Z}\phi dZ\right). \tag{B4b}$$

From a view point of the current second-order KdV theory [e.g., *Lamb and Yan*, 1996; *Holloway et al.*, 1999; *Grimshaw et al.*, 2002], (B3) and (B4) implicitly use orthogonality between the structure function for first-order nonlinear effects (commonly denoted as T_n [*Holloway et al.*, 1999; *Grimshaw et al.*, 2002]) and the mode of interest ϕ as the auxiliary condition. Since the choice of auxiliary condition is considered to be arbitrary, our implicit choice is consistent with the current second-order KdV theory.

The solitary wave solution provides the final link between $\hat{w}$ and solitary-wave amplitude A. The soliton solution to the Gardner equation [e.g., *Helfrich and Melville*, 2006] is

$$\eta' = \frac{(2+qA')A'}{-qA' + 2(1+qA')\cosh^2\Theta}, \tag{B5a}$$

$$\eta' = \frac{\alpha}{c}\hat{\eta},\ A' = \frac{\alpha}{c}A,\ q = \frac{\alpha_1 c}{\alpha^2},\ \Theta = \kappa(x - c_{sw}t), \tag{B5b}$$

$$c_{sw} = c\left(1 + \frac{A'}{3}\left(1 + \frac{qA'}{2}\right)\right),\ \kappa = \sqrt{\frac{c}{12\beta}A'\left(1 + \frac{qA'}{2}\right)}. \tag{B5c}$$

Substituting (B5) into (B4a) yields the relationship between $\hat{w}$ and A, and a simplified formula can be obtained by Taylor series expansion. Noting that the extrema of $\partial\eta'/\partial x = \partial\eta'/\partial\xi$ are located at $\Theta_e = \tanh^{-1}(\pm 1/\sqrt{3})$, η' and $\partial\eta'/\partial\xi$ in terms of small A' at $\Theta = \Theta_e$ are

$$\eta' \sim \frac{1}{\cosh^2\Theta_e}A' \equiv f_0 A', \tag{B6a}$$

$$\frac{\partial\eta'}{\partial\xi} \sim -2\frac{\tanh\Theta_e}{\cosh^2\Theta_e}\kappa A' - \frac{(2-\cosh^2\Theta_e)\tanh\Theta_e}{\cosh^4\Theta_e}\kappa q A'^2 \equiv (f_1 + f_2 qA')\kappa A'. \tag{B6b}$$

By substituting (B5) and (B6) into (B4a) and keeping the terms up to $O(A'^{5/3})$, we get

$$\sqrt{\frac{12\alpha^2\beta}{c^3}}\frac{\hat{w}}{c} \sim f_1\left(\frac{\alpha A}{c}\right)^{3/2}+\left\{\left(\frac{1}{3}+\frac{q}{4}-\frac{cN_B}{\alpha h}f_0\right)f_1+qf_2\right\}\left(\frac{\alpha A}{c}\right)^{5/2}. \tag{B7}$$

To apply the above method to the model output, we calculate ϕ, c, α, α_1, and β using the background stratification in Figure 3a and the local water depth $H(\vec{x})$ at each horizontal grid point. Then, we calculate $\hat{w}$ from the model output using (B3), find the maximum modal vertical velocity difference within an ISW $\Delta\hat{w}$, and use $\Delta\hat{w}/2$ instead of $\hat{w}$ in (B7) to reduce the error due to "background" vertical velocity not associated with the ISW.

Acknowledgments

We thank two anonymous reviewers for constructive comments, and Steve Buchan for proof-reading. K.S. was partially supported by funding from Research Connections grant from Australian Department of Industry, Innovation, and Science, RPS MetOcean Pty Ltd. in Perth, Australia, and CSIRO during this study. We appreciate the provision of computational resources by RPS MetOcean and CSIRO, and Climate Data Operator by Max Planck Institute for Meteorology (https://code.zmaw.de/projects/cdo). The source code of MITgcm and the Thermodynamic Equation of Seawater-2010 are freely available from http://mitgcm.org/and http://www.teos-10.org/, respectively. SRTM15_PLUS, TPXO8-atlas, and World Ocean Atlas 2013 were freely downloaded from Scripps Institution of Oceanography (http://topex.ucsd.edu/www_html/srtm30_plus.html), Oregon State University (http://volkov.oce.orst.edu/tides/tpxo8_atlas.html), and NOAA (https://www.nodc.noaa.gov/OC5/woa13/woa13data.html), respectively. The model outputs are available from Shimizu and Nakayama [2017].

References

Adcroft, A., C. Hill, and J. Marshall (1997), Representation of topography by shaved cells in a height coordinate ocean model, *Mon. Weather Rev.*, *125*, 2293–2315.

Becker, J. J., et al. (2009), Global bathymetry and elevation data at 30 arc seconds resolution: SRTM30_PLUS, *Mar. Geod.*, *32*, 355–371.

Benjamin, B. (1966), Internal waves of finite amplitude and permanent form, *J. Fluid Mech.*, *25*, 241–270.

Benney, D. J. (1966), Long non-linear waves in fluid flows, *J. Math. Phys.*, *45*, 52–63.

Egbert, G. D., and S. Y. Erofeeva (2002), Efficient inverse modeling of barotropic ocean tides, *J. Atmos. Oceanic Technol.*, *19*, 183–204.

Funakoshi, M. (1980), Reflection of obliquely incident solitary waves, *J. Phys. Soc. Jpn.*, *49*, 2371–2379.

Gabl, E. F. (1986), Requirements for three-dimensional resonant interaction of ion-acoustic solitons, *Phys. Fluids*, *29*, 1737–1738.

Gerkema, T., J. T. F. Zimmerman, L. R. M. Maas, and H. van Haren (2008), Geophysical and astrophysical fluid dynamics beyond the traditional approximation, *Rev. Geophys.*, *46*, RG2004, doi:10.1029/2006RG000220.

Gill, A. E. (1982), *Atmosphere-Ocean Dynamics*, 662 pp., Academic, San Diego, Calif.

Griffiths, S. D., and R. H. J. Grimshaw (2007), Internal tide generation at the continental shelf modeled using a modal decomposition: Two-dimensional results, *J. Phys. Oceanogr.*, *37*, 428–451, doi:10.1175/JPO3068.1.

Grimshaw, R., E. Pelinovsky, and O. Poloukhina (2002), Higher-order Korteweg-de Vries models for internal solitary waves in a stratified shear flow with a free surface, *Nonlinear Proc. Geophys.*, *9*, 221–235.

Grimshaw, R., C. Guo, K. Helfrich, and V. Vlasenko (2014), Combined effect of rotation and topography on shoaling oceanic internal solitary waves, *J. Phys. Oceanogr.*, *44*, 1116–1132, doi:10.1175/JPO-D-13-0194.1.

Guo, C., X. Chen, V. Vlasenko, and N. Stashchuk (2011), Numerical investigation of internal solitary waves from the Luzon Strait: Generation process, mechanism and three-dimensional effects, *Ocean Modell.*, *38*, 203–216, doi:10.1016/j.ocemod.2011.03.002.

Helfrich, K. R., and W. K. Melville (2006), Long nonlinear internal waves, *Annu. Rev. Fluid Mech.*, *38*, 395–425.

Holloway, P. E., E. Pelinovsky, T. Talipova, and B. Barnes (1997), A nonlinear model of internal tide transformation on the Australian North West Shelf, *J. Phys. Oceanogr.*, *27*, 871–896.

Holloway, P. E., E. Pelinovsky, and T. Talipova (1999), A generalized Korteweg-de Vries model of internal tide transformation in the coastal zone, *J. Geophys. Res.*, *104*, 18,333–18,350.

Hyder, P., D. R. G. Jeans, E. Cauquil, and R. Nerzic (2005), Observations and predictability of internal solitons in the northern Andaman Sea, *Appl. Ocean Res.*, *27*, 1–11.

Jackson, C. (2004), *An Atlas of Internal Solitary-Like Waves and Their Properties*, 2nd ed., 560 pp., Global Ocean Assoc., Alexandria, Va. [Available at http://www.internalwaveatlas.com.]

Jackson, C. (2007), Internal wave detection using the Moderate Resolution Imaging Spectroradiometer (MODIS), *J. Geophys. Res.*, *112*, C11012, doi:10.1029/2007JC004220.

Johnson, R. S. (1982), On the oblique interaction of a large and a small solitary wave, *J. Fluid Mech.*, *120*, 49–70.

Kadomtsev, B. B., and V. I. Petviashivili (1970), On the stability of solitary waves in weakly dispersing media, *Sov. Phys. Dokl.*, *15*, 539–541.

Kako, F., and N. Yajima (1982), Interaction of ion-acoustic solitons in multi-dimensional space II, *J. Phys. Soc. Jpn.*, *51*, 311–322.

Kaup, D. J. (1981), Nonlinear resonances and colliding spherical ion-acoustic solitons, *Physica D*, *2*, 389–394.

Kelly, S. M., J. D. Nash, K. I. Martini, M. H. Alford, and E. Kunze (2012), The cascade of tidal energy from low to high modes on a continental slope, *J. Phys. Oceanogr.*, *42*, 1217–1232, doi:10.1175/JPO-D-11-0231.1.

Klymak, J. M., and J. N. Moum (2003), Internal solitary waves of elevation advancing on a shoaling shelf, *Geophys. Res. Lett.*, *30*(20), 2045, doi:10.1029/2003GL017706.

Klymak, J. M., R. Pinkel, C.-T. Liu, A. K. Liu, and L. David (2006), Prototypical solitons in the South China Sea, *Geophys. Res. Lett.*, *33*, L11607, doi:10.1029/2006GL025932.

Kodama, Y. (2010), KP solitons in shallow water, *J. Phys. A: Math. Theor.*, *43*, 434004, doi:10.1088/1751-8113/43/43/434004.

Kodama, Y., and H. Yeh. (2016), The KP theory and Mach reflection, *J. Fluid Mech.*, *800*, 766–786, doi:10.1017/jfm.2016.422.

Lamb, K. G. (2014), Internal wave breaking and dissipation mechanisms on the continental slope/shelf, *Annu. Rev. Fluid Mech.*, *46*, 231–254, doi:10.1146/annurev-fluid-011212-140701.

Lamb, K. G., and L. Yan (1996), The evolution of internal wave undular bores: Comparisons of a fully nonlinear numerical model with weakly nonlinear theory, *J. Phys. Oceanogr.*, *26*, 2712–2734.

Li, W., H. Yeh, and Y. Kodama (2011), On the Mach reflection of a solitary wave: Revisited, *J. Fluid Mech.*, *672*, 326–357, doi:10.1017/S0022112010006014.

Locarnini, R. A., et al. (2013a), World Ocean Atlas 2013, volume 1: Temperature, in *NOAA Atlas NESDIS 73*, edited by S. Levitus, 40 pp., NOAA, Silver Spring, Md.

Locarnini, R. A., et al. (2013b), World Ocean Atlas 2013, volume 2: Salinity, in *NOAA Atlas NESDIS 73*, edited by S. Levitus, 39 pp., NOAA, Silver Spring, Md.

Lonngren, K. E. (1983), Soliton experiments in plasmas, *Plasma Phys.*, *25*, 943–982.

Marshall, J., A. Adcroft, C. Hill, L. Perelman, and C. Heisey (1997), A finite-volume, incompressible Navier-Stokes model for studies of the ocean on parallel computers, *J. Geophys. Res.*, *102*, 5753–5766.

Maxworthy, T. (1980), On the formation of nonlinear internal waves from the gravitational collapse of mixed regions in two and three dimensions, *J. Fluid Mech.*, *96*, 47–64.

McDougall, T. J., and P. M. Baker (2011), Getting started with TEOS-10 and the Gibbs Seawater oceanographic toolbox, *Rep. SCOR/IAPSO WG127*, 28 pp. [Available at http://www.teos-10.org/pubs/Getting_Started.pdf.]

Melville, W. K. (1980), On the Mach reflexion of a solitary wave, *J. Fluid Mech.*, *98*, 285–297.

Miles, J. W. (1977), Resonantly interacting solitary waves, *J. Fluid Mech.*, *79*, 171–179.

Miles, J. W. (1978), An axisymmetric Boussinesq wave, *J. Fluid Mech.*, *84*, 181–191.

Miles, J. W. (1980), Solitary waves, *Annu. Rev. Fluid Mech.*, *12*, 11–43.

Nakamura, Y. (1982), Experiments on ion-acoustic solitons in plasma, *IEEE Trans. Plasma Sci.*, *10*, 180–195.

New, A. L., J. M. Magalhaes, and J. C. B. da Silva (2013), Internal solitary waves on the Saya de Malha bank of the Mascarene Plateau: SAR observations and interpretation, *Deep Sea Res., Part I*, *179*, 50–61, doi:10.1016/j.dsr.2013.05.008.

Oikawa, M., and H. Tsuji (2006), Oblique interactions of weakly nonlinear long waves in dispersive systems, *Fluid Dyn. Res.*, *38*, 868–898, doi:10.1016/j.fluiddyn.2006.07.002.

Osborne, A. R., and T. L. Burch (1980), Internal solitons in the Andaman Sea, *Science*, *208*, 451–460.

Peterson, P., T. Soomere, J. Engelbrecht, and E. van Groesen (2003), Soliton interaction as a possible model for extreme waves in shallow water, *Nonlinear Proc. Geophys.*, *10*, 503–510.

Reeder, D. B., L. Y. S. Chiu, and C-F. Chen (2010), Experimental evidence of horizontal refraction by nonlinear internal waves of elevation in shallow water in the South China Sea: 3D versus Nx2D acoustic propagation modeling, *J. Comput. Acoust.*, *18*, 267–278.

Reeder, D. B., B. B. Ma, and Y. J. Yang (2011), Very large subaqueous sand dunes on the upper continental slope in the South China Sea generated by episodic, shoaling deep-water internal solitary waves, *Mar. Geol.*, *279*, 12–18.

Scotti, A., and J. Pineda (2004), Observation of very large and steep internal waves of elevation near the Massachusetts coast, *Geophys. Res. Lett.*, *31*, L22307, doi:10.1029/2004GL021052.

Segur, H., and A. Finkel (1985), An analytical model of periodic waves in shallow water, *Stud. Appl. Math.*, *73*, 183–220.

Shimizu, K. (2011), A theory of vertical modes in multilayer stratified fluids, *J. Phys. Oceanogr.*, *41*, 1694–1707, doi:10.1175/2011JPO4546.1.

Shimizu, K., and K. Nakayama (2017), Effects of topography and Earth's rotation on the oblique interaction of internal solitary-like waves in the Andaman Sea, *J. Geophys. Res. Oceans*, doi:10.1002/2017JC012888, in press.

Small, J. (2001a), A nonlinear model of the shoaling and refraction of internal solitary waves in the ocean. Part I: Development of the model and investigation of the shoaling effect, *J. Phys. Oceanogr.*, *31*, 3163–3183.

Small, J. (2001b), A nonlinear model of the shoaling and refraction of internal solitary waves in the ocean. Part II: Oblique refraction across a continental slope and propagation over a sea mount, *J. Phys. Oceanogr.*, *31*, 3184–3199.

Soomere, T. (2004), Interaction of Kadmotsev-Petviashvili solitons with unequal amplitudes, *Phys. Lett. A*, *332*, 74–81.

Tanaka, M. (1993), Mach reflection of a large-amplitude solitary wave, *J. Fluid Mech.*, *248*, 637–661.

Tsuji, H., and M. Oikawa (1993), Two-dimensional interaction of internal solitary waves in a two-layer fluid, *J. Phys. Soc. Jpn.*, *62*, 3881–3892.

Tsuji, H., and M. Oikawa (2007), Oblique interaction of solitons in an extended Kadomtsev-Petviashvili equation, *J. Phys. Soc. Jpn.*, *76*, 084401, doi:10.1143/JPSJ.76.084401.

Tsukabayashi, I., and Y. Nakamura (1981), Resonant interactions of cylindrical ion-acoustic solitons, *Phys. Lett. A*, *85*, 151–154.

Vitousek, S., and O. B. Fringer (2011), Physical vs. numerical dispersion in nonhydrostatic ocean modeling, *Ocean Modell.*, *40*, 72–86, doi:10.1016/j.ocemod.2011.07.002.

Vlasenko, V., and N. Stashchuk (2007), Three-dimensional shoaling of large-amplitude internal waves, *J. Geophys. Res.*, *112*, C11018, doi:10.1029/2007JC004107.

Vlasenko, V., J. C. S. Garrido, N. Stashchuk, J. G. Lafuente, and M. Losada (2009), Three-dimensional evolution of large-amplitude internal waves in the Strait of Gibraltar, *J. Phys. Oceanogr.*, *39*, 2230–2246, doi:10.1175/2009JPO4007.1.

Vlasenko, V., N. Stashchuk, M. E. Inall, and J. E. Hopkins (2014), Tidal energy conversion in a global hot spot: On the 3-D dynamics of baroclinic tides at the Celtic Sea shelf break, *J. Geophys. Res. Oceans*, *119*, 3249–3265, doi:10.1002/2013JC009708.

Wang, C., and R. Pawlowicz (2012), Oblique wave-wave interactions of nonlinear near-surface internal waves in the Strait of Georgia, *J. Geophys. Res.*, *117*, C06031, doi:10.1029/2012JC008022.

Wang, Y.-H., C.-F. Dai, and Y.-Y. Chen (2007), Physical and ecological processes of internal waves on an isolated reef ecosystem in the South China Sea, *Geophys. Res. Lett.*, *34*, L18609, doi:10.1029/2007GL030658.

Xie, X. H., Y. Cuypers, P. Bouruet-Aubertot, B. Ferron, A. Pichon, A. Lourenço, and N. Cortes (2013), Large-amplitude internal tides, solitary waves, and turbulence in the central Bay of Biscay, *Geophys. Res. Lett.*, *40*, 2748–2754, doi:10.1002/grl.50333.

Xue, J., H. C. Graber, B. Lund, and R. Romeister (2013), Satellite observation of a zipper-like internal wave-wave interaction pattern in the mid-Atlantic Bight, *Int. Geosci. Remote Sens.*, 1571–1574, doi:10.1109/IGARSS.2013.6723089.

Yeh, H., W. Li, and Y. Kodama (2010), Mach reflection and KP solitons in shallow water, *Eur. Phys. J. Spec. Top.*, *185*, 97–111, doi:10.1140/epjst/e2010-01241-0.

Zabusky, N. J., and M. D. Kruskal (1965), Interactions of "solitons" in a collisionless plasma and the recurrence of initial states, *Phys. Rev. Lett.*, *15*, 240–243.

Ze, F., N. Hershkowitz, and K. E. Lonngren (1980), Oblique collision of ion-acoustic solitons, *Phys. Fluids*, *23*, 1155–1163.

Zhang, Z., O. B. Fringer, and S. R. Ramp (2011), Three-dimensional, nonhydrostatic numerical simulation of nonlinear internal wave generation and propagation in the South China Sea, *J. Geophys. Res.*, *116*, C05022, doi:10.1029/2010JC006424.

Zhou, X., and R. Grimshaw (1989), The effect of variable currents on internal solitary waves, *Dyn. Atmos. Oceans*, *14*, 17–39.